Rock Mechanics
and Rock Engineering 24, 133—153

**Rock Mechanics and Rock Engineering**



# A Phenomenological Failure Criterion for Brittle Rock

By

**Z. Ouyang**[1] and **D. Elsworth**[2]

[1] Department of Mining Engineering, Wuhan Steel and Iron University, Wuhan, People's Republic of China

[2] Department of Mineral Engineering, Pennsylvania State University, U.S.A., and Waterloo Centre for Groundwater Research, University of Waterloo, Canada

**Summary**

A phenomenological model is developed to represent failure in intact media as a consequence of shear-band formation. A stepped arrangement of connected flaws is assumed to be distributed within a planar shear-band inclined with respect to the applied deviatoric stresses. The flaws within the shear-band isolate a series of wedges that transmit tractions across the pre-failure zone. Gross stress transmission is controlled by static equilibrium with spatial stress inhomogeneity modulated through the distribution of flaws in the continuum adjacent to the shear-band. Under increased confinement, flaw closure beyond the shear-band results in a more homogeneous transmission of normal tractions across the failure plane. This stress dependent transition is based on physical arguments, related to mean flaw closure, to yield a distribution coefficient, $W$, that is controlled by macroscopic flaw rigidity, $B$. The model is able to replicate the power law dependency of ultimate strength with confining stress that is commonly observed. The model is specifically calibrated against experimental data for Daye marble. The phenomenological coefficients describing the failure process appear as material constants.

## 1. Introduction

Failure in brittle rock is initiated by the extension of existing microcracks, creation of fresh crack surface area, and consequent dissipation of energy. The onset of microcrack extension, as predicted through fracture mechanics, indicates the development of zones of irreversible deformation within the body and may be viewed as a precursor to failure. Peak strength, however, is only reached as a later result of crack coalescence on a macroscopic scale. Consequently, the prediction of flaw coalescence into a continuous shear-band is a critical factor in determining ultimate failure of intact rock or rock masses. A wealth of laboratory results indicate the control that microcracks exert on macroscopic failure of brittle materials

originating with the seminal deductions of Griffith (1921, 1924). Subsequently, many investigators have addressed the strain rate and stress level sensitivity of microcrack development and propagation to indicate that macrofractures result from the interaction and coalescence of microcracks rather than the existence of a single pre-existing discontinuity (Brace and Bombolakis, 1963; Bombolakis, 1968; Hoek and Bieniawski, 1965; Bieniawski, 1966).

Investigating the compressive behaviour of Westerly granite, Wu and Thomsen (1975) identified three distinct stages of progressive failure. Initially, pre-existing cracks are either closed or opened, depending on inclination to the deviatoric stresses. Cracks near-perpendicular to the major stress axis are closed and those near-parallel are opened. As the principal stress exceeds half of the failure stress, microcracks propagate in the major principal direction (Brace et al., 1966; Peng and Johnson, 1972; Tapponier and Brace, 1976; Kranz, 1979 a,b; Wang, 1982) forming an inclined zone of intensive deformation (Peng and Johnson, 1972; Wang, 1982; Dey and Wang, 1981; Hallbauer et al., 1973; Scholz, 1968 a,b; Liu and Livanos, 1976). With further compression, the cracks anastomose as a result of interaction in their respective induced stress fields.

Both en échelon and en passant microcrack geometries have been observed in overlap (Kranz, 1979 a,b) as a result of crack-crack and crack-pore interactions in granite. Excepting the overlapped crack-tip regions, the differences between the two types of microcracks disappear following coalescence as a serrated shear plane develops with additional loading. Swain et al. (1974) show how an en passant interaction can eventually produce a characteristic serrated crack with en échelon appearance. The anastomosing of microcracks is approximately perpendicular to maximum compression (Nesetova and Lajtai, 1973). Fonseka et al. (1985) use both scanning electron microscope and microseismic observations to study the growth of cracks in samples at various compressional loads up to failure and determined similar microcrack interactions. Close to the ultimate failure stress, this fracture plane can grow by stepwise joining of existing microcrack tips to form much larger serrated cracks (Kranz, 1979b; Fonseka et al., 1985). Similar studies (Bombolakis, 1968; Bieniawski, 1966) using crack arrays show that, provided adjacent cracks are in close proximity, cracks coalesce in both the direction of greatest stress and in the direction perpendicular to it. These microcracks are related to point contacts between grains (Kranz, 1979a; Batzle et al., 1979) and represent regions of isolated stress concentration.

Numerous researchers have postulated mechanisms and developed criteria for failure. Wiebols and Cook (1968) suggest that the failure occurs when the inelastic shear strain of macrocracks (sliding in the manner proposed by McClintock and Walsh (1962)) reaches some critical value. Brady (1969 a,b) proposed that failure occurs when the total volumetric strain due to microcracks reaches some critical value. Lundborg (1974) proposed a statistical theory based on subdividing a rock into many regions with a distribution of strengths.

Peng and Johnson (1972) and Janach (1977) use a small beam to model the region between two axially-oriented microcracks. Dey and Wang (1981) propose the inhomogeneity model to provide an explanation based on a mismatch in elastic properties of neighbouring grains and the wedging process caused by a point contact between grains.

In this paper a simple phenomenological model is presented to incorporate many of the observed failure phenomena described above. Specifically, failure is described through formation of a diagonal shear-band comprising an inclined serrated plane that will disrupt the previous near-homogeneous stress state within the sample and describe the localization process. Evidence of shear band formation is commonly apparent following brittle failure through the presence of an undulating fracture plane supporting a particulate coating. It is suggested in the following that the thickness of the developing shear-band is of the order of the grain or crystal diameter or similar dimension corresponding to the intergranular flaw size. Despite the fine scale of this feature, its presence is sufficient to significantly modify the stress distribution in the sample in a stress dependent manner. The stress dependent strength of the solid follows directly from the physical argument requiring that the homogeneity of stress transmission is controlled by closure of preexisting flaws. The correspondence with laboratory data suggests that the phenomenological model provides a plausible explanation of the failure process in the absence of more detailed microscopic failure data.

## 2. Wedge Model

There is ample evidence (Tapponnier and Brace, 1976; Hallbauer, 1973) that the process which determines the strength of brittle rocks under triaxial compression is not of a shear type. Failure begins following the collapse of microstructure that has been previously weakened by predominantly axial microcracking. The collapse results from structural instability concentrated along a plane which, in subsequent stages, becomes a fault at low angle to the major principal compression. Once formed, shear motion induces a complex loading of the surrounding rock.

When stresses are close to ultimate rock strength, cracks parallel and perpendicular to the major principal stress direction deform and extend to form a serrated failure plane connected through crack tips. This arrangement is illustrated as a shear-band in Fig. 1 from which a single free-body wedge is isolated in Fig. 2. The wedge geometry is loaded only at the tips of connected cracks. Assuming that $P_1$ and $P_2$ are respectively normal and shear tractions on a wedge element, the radial stress distribution ($\sigma_r$) within this wedge can be expressed (Timoshenko and Goodier, 1970) as

$$\sigma_r = (K_1 P_1 \sin\theta + K_2 P_2 \cos\theta)(1/r) \quad (1)$$

where $r$ = radius of interest, $\theta$ = polar angle relative to the macroscopic shear-band, $K_1 = 4/(\pi+2)$, and $K_2 = 4/(\pi-2)$.

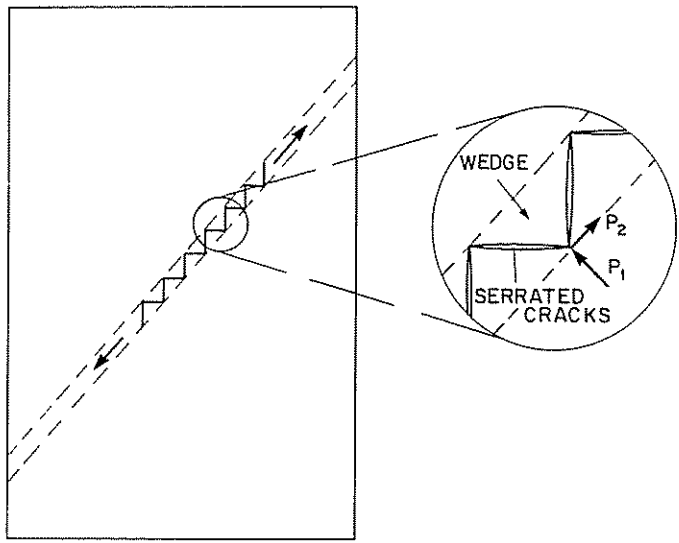


**Fig. 1.** Formation of a diagonal array of wedge elements defining the serrated failure plane

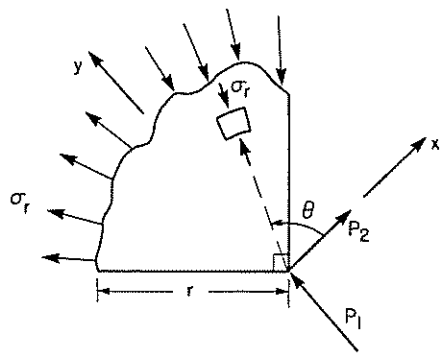


**Fig. 2.** Free-body wedge geometry from the serrated failure plane

A single isolated transverse or axial crack does not affect the stability of the entire rock structure. Ultimate failure results from the mutual interaction of critically oriented and located cracks. This interaction may contribute to the formation of a diagonal array of wedge free-bodies as previously illustrated in Fig. 1. In reality, the wedge elements will not be of uniform size, but will conform to some distribution possessing a mean size. If a specimen is separated along the serrated microcracks and assuming: (i) that $m$ wedge elements exist within a unit length along the potential failure

plane; (ii) that internal stresses are concentrated only at the tips of wedge elements, as illustrated in Fig. 3 and; (iii) that the medium beyond the plane is a uniform continuum, the conditions for equilibrium can be expressed by the Eqs.

$$2\,m P_1 = \frac{1}{2}(\sigma_1 + \sigma_3) + \frac{1}{2}(\sigma_1 - \sigma_3)\cos 2\Phi \tag{2a}$$

$$2\,m P_2 = \frac{1}{2}(\sigma_1 - \sigma_3)\sin 2\Phi, \tag{2b}$$

where $(\sigma_1, \sigma_3)$ are the major and minor principal stresses and $\Phi$ is the angle of a potential failure plane.

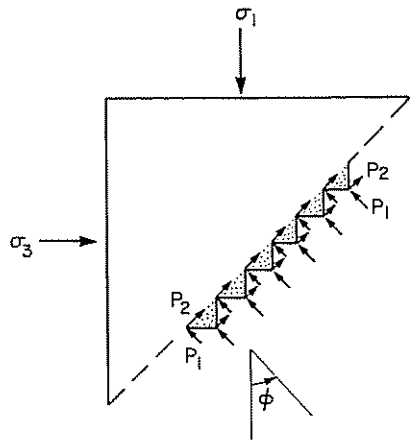


**Fig. 3.** Traction at the connected points of the serrated microcracks

The medium exterior to the "failure plane" is not a uniform continuum with the result that local stress inhomogeneities, caused by microcracks and minerals of differing elastic modulii, must be accommodated in a statistically equivalent manner. The traction distribution over the tips of wedge elements in Fig. 3 will be redistributed by both microcracks and modulii inhomogeneities beyond the failure zone (Tapponnier and Brace, 1976; Kranz 1979a; Batzle et al., 1979). As a result, the distribution of the resultant traction will be non-uniform.

It is suggested that macroscopic redistribution of stresses will accompany small deformations over the failure zone. Small shear deformations will precipitate a homogenization of shear stresses ($P_2$) along the potential failure plane but normal traction magnitudes will remain ostensibly unchanged and inhomogeneous as a result of the flaw distribution exterior to the failure zone. To accommodate this phenomenon, the coefficient of stress inhomogeneity, $W$, is proposed to represent the controlling influence of "higher than average" normal tractions ($P_1$) on the ensuing failure process. The coefficient $W$ is bounded by zero and unity and phys-

ically represents the proportion of wedge apices transferring normal tractions across the failure zone. Consequently Eq. (2) may be rewritten as

$$2\,m\,WP_1 = \frac{1}{2}(\sigma_1 + \sigma_3) + \frac{1}{2}(\sigma_1 - \sigma_3)\cos 2\Phi \tag{3a}$$

$$2\,m\,P_2 = \frac{1}{2}(\sigma_1 - \sigma_3)\sin 2\Phi \tag{3b}$$

### *2.1 Inhomogeneous Stresses*

As discussed previously, the value of $W$ is generally a function of the density and closure of microcracks exterior to the failure zone and the modulus contrast of the component minerals. The local stress distribution is extremely complex and consequently analytical description of the stress inhomogeneity coefficient $W$, at microscale, is impossible. Alternatively, a mixed analytical and empirical approach may be used to determine $W$ directly. For a specific rock or material, the initial microcrack density and modulus variability are fixed, but unknown. In the course of loading, the slight microcracking that occurs beyond the potential failure plane is neglected and it is assumed that minerals of different elastic moduli will be unchanged by the loading process. Consequently, changes in the coefficient $W$ depend entirely on microcrack closure exterior to the failure zone. The coefficient $W$ may therefore be divided into two parts: the first part ($W_I$) is a function of inherent properties of a rock (i. e., the minerals and microcrack density) and is not related to the loading process. The magnitude of $W_I$ can be indirectly determined from strength test data that will be discussed later. The second part ($W_{II}$) is a function of the microcrack closure immediately prior to the macrofailure of the rock. $W_{II}$ is affected only by the imposed stress state surrounding a microcrack and may be determined from consideration of elastic (pre-failure) crack closure. From the preceding, the stress inhomogeneity coefficient $W$ can be specified by the relation

$$W = W_I + W_{II}. \tag{4}$$

If the elliptic flaw identified in Fig. 4 is used to represent a microcrack, it can be assumed that $W_{II}$ is proportional to mean microcrack closure as:

$$W_{II} = h\,(\Delta b_{ave}/b) \tag{5}$$

where $h$ is a constant and $\Delta b_{ave}$ is an average value of the microcrack closure at the ends of minor axis, $b$. The modulating parameter $W$ varies between 0 and 1. If $W=1$, the parts beyond the potential failure plane represent a uniform continuum and each tip of the wedge elements is subject to a normal traction $P$. In the special case of $W=0$, the appropriate stress state is uniaxial tensile stress, as will be discussed later. The special case of $W=0$ can be considered as an extension of the wedge model.

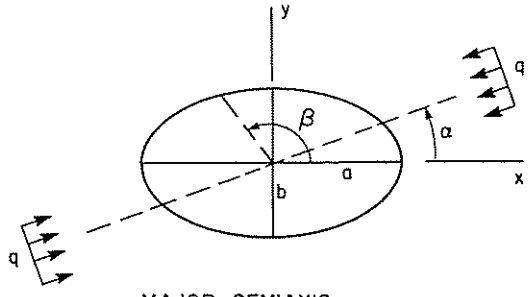


Fig. 4. A flat elliptical hole

For the idealized elliptical flaw within an uniaxial stress field ($q$), illustrated in Fig. 4, closure ($v$) is given by

$$v = Rq(1 - \mu^2)(1 + n - 2\cos 2\alpha)/E, \tag{6}$$

where $R = (a + b)/2$ and $n = (a - b)/(a + b)$, as described in Appendix 1. Here, $a$ and $b$ are the flaw semi-major and semi-minor axes, respectively, and $\mu$ is the Poisson ratio. Of particular interest is the displacement at an angle $\alpha = \pi/2$ to the $x$ axis representing closure across the minor axis. Superposition enables a general stress state to be represented, as illustrated in Fig. 5, to yield closure ($\Delta b$) due to the principal stress state as

$$\Delta b = (1 - \mu^2)[(2a + b)\sigma_y - b\sigma_x]/E. \tag{7}$$

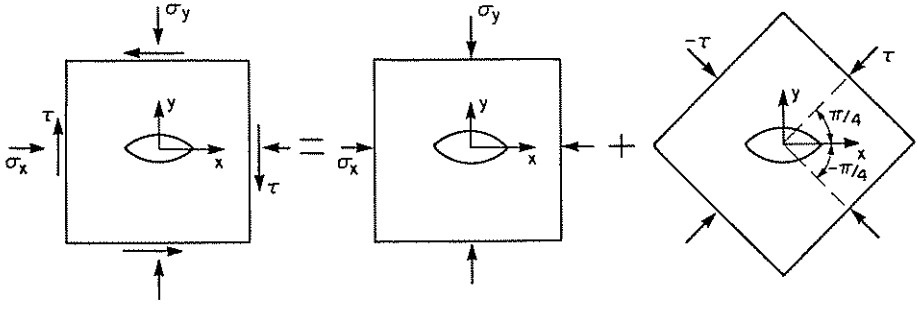


Fig. 5. Superposition of stress components

Assuming that microcracks beyond the potential failure zone are both randomly located and continuously distributed, the average closure $\Delta b_{ave}$ may be evaluated. Defining the angle between the major principal stress $\sigma_1$ and $\sigma_y$ of Fig. 5 as $\delta$ and substituting the major and minor principal stresses, the average displacement $\Delta b_{ave}$ is then

$$\Delta b_{\text{ave}} = \frac{1}{2\pi} \int_0^{2\pi} \Delta b \, d\delta = a(1-\mu^2)(\sigma_1 + \sigma_3)/E \tag{8}$$

Substitution of Eq. (8) into Eq. (5) and Eq. (4) yields

$$W = B(\sigma_1 + \sigma_3) + W_1, \tag{9}$$

where the parameter $B = ha(1-\mu^2)/(Eb)$ in which $h$ is inversely proportional to microcrack density. Direct prediction of the statistical constants, $h$, $a$, and $b$ of the parameter $B$ may be difficult. Fortunately, $B$ and $W_1$ can be indirectly determined by rock strength data following introduction of another expression for $W$, later.

Following full microcrack closure under external compressive loading, the material beyond the potential failure plane is presumed to become a continuum as $W$ approaches unity. For this reason, the inhomogeneous stress coefficient ($W$) assumes one of two possible magnitudes as determined by the prevailing stress regime. These are given as

$$W = \begin{cases} B(\sigma_1 + \sigma_3) + W_1, & -W_1/B \le \sigma_1 + \sigma_3 \le (1 - W_1)/B \quad (9\text{a}) \\ 1, & \sigma_1 + \sigma_3 > (1 - W_1)/B \quad (9\text{b}) \end{cases}$$

### 2.2 *Criterion for the Formation of a Potential Failure Plane*

A criterion must be applied to the microscopic or macroscopic stress regime to define formation of a failure plane. Previously, Janach (1977) assumed that the concentration of elements along a diagonal failure plane minimize the total dilative work for the specific confining stress $\sigma_3$. Alternatively, Woronow (1975) proposed that the local major principal stress $\sigma_1$ at failure should reach a minimum in the development of the failure plane and was able to corroborate this behaviour with experimental results. An alternative Woronow's macroscopic condition is posed at the microscopic scale in this work. Woronow's condition for a failure plane may be extended to the microscale by stating that, *the formation of the failure plane will minimize the tensile stress $\sigma_r$ on the edge of a wedge element.*

Of particular interest, therefore, are the tensile stresses $\sigma_r$ on the edge of a wedge element. As illustrated in Figs. 2 and 3, all stress components are in assumed positive directions so that the edge at $\theta = 3\pi/4$ is potentially under a tensile stress state. At the point contacts, of wedge apices, tensile microfailure may occur allowing Eq. (1) to be rewritten as

$$\sigma_r = (K_1 P_1 - K_2 P_2)/(r\sqrt{2}) \tag{10}$$

Combining Eq. (3a) and (3b) with Eq. (10), yields

$$\sigma_r = \frac{K_1}{2\sqrt{2}\, rm\, W}\left[\frac{\sigma_1 + \sigma_3}{2} + \frac{\sigma_1 - \sigma_3}{2}\cos 2\Phi - \frac{K_2 W}{K_1}\left(\frac{\sigma_1 - \sigma_3}{2}\sin 2\Phi\right)\right]. \tag{11}$$

Evaluation of derivatives through second order (see Appendix 2) for Eq. (11) provides an explanation of the preferred formation of a potential failure plane. Setting $d\sigma_r/d\Phi = 0$, the result becomes

$$\operatorname{tg} 2\Phi = -K_2 W/K_1 \qquad 0 \leq W \leq 1 \tag{12}$$

or

$$W = -K_1 \operatorname{tg} 2\Phi/K_2 \qquad 0 \leq W \leq 1 \tag{13}$$

The preferred angle of a potential failure plane is given by further discussion of Eq. (12) in Appendix 2 as

$$\Phi = \pi/2 - \varepsilon, \tag{14}$$

where $\varepsilon$ is $\frac{1}{2}\operatorname{arctg}(K_2 W/K_1)$ ($\leq \pi/4$). The tensile stress $\sigma_r$ at this angle proves to be a minimum.

According to Eq. (13), evaluation of the microconstants in $B$ (of Eq. (9a) such as $h$, $a$, $b$, etc.) may be avoided. The two constants $B$ and $W_1$ may be determined from a minimum of two triaxial tests exhibiting different deviatoric stresses at failure.

## 3. Failure Criterion

The empirical Mohr failure criterion implicitly accommodates the variety of microscopic phenomena described previously. It does not, however, enable a prediction of ultimate strength to be made from knowledge of physical parameters such as flaw density. Fortunately, the Mohr criterion does provide a foundation from which a criterion may be theoretically extended. Considering the stress space of Fig. 6, the partial derivatives $\partial \tau_\Phi/\partial \sigma_\Phi$ and $\partial \sigma_1/\partial \sigma_3$ are related as (Vutukuri et al., 1974)

$$\frac{\partial \tau_\Phi}{\partial \sigma_\Phi} = -\frac{1}{\operatorname{tg} 2\Phi} = \frac{\dfrac{\partial \sigma_1}{\partial \sigma_3} - 1}{2\left(\dfrac{\partial \sigma_1}{\partial \sigma_3}\right)^{1/2}}, \tag{15}$$

where $\tau_\Phi$ and $\sigma_\Phi$ are, respectively, shear and normal stresses on a failure plane. Clearly, $\tau_\Phi$ is $2\, m P_2$ and $\sigma_\Phi$ is $2\, m W P_1$.

Assuming that at failure, the major principal stress is $\sigma_1$ and the minor principal stress is $\sigma_3$, then according to Fig. 6

$$\left(\frac{\sigma_1 + \sigma_3}{2} - \sigma_\Phi\right)^2 + \tau_\Phi^2 = \left(\frac{\sigma_1 - \sigma_3}{2}\right)^2. \tag{16}$$

Taking the derivative of $\sigma_1$ with respect to $\sigma_3$ from Eq. (16) yields the solution for $\sigma_\Phi$ as

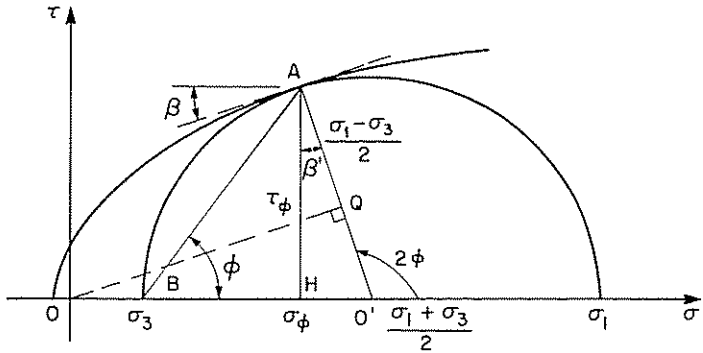


Fig. 6. Geometry of a Mohr envelope

$$\sigma_\Phi = \sigma_3 + \frac{\sigma_1 - \sigma_3}{\frac{\partial \sigma_1}{\partial \sigma_3} + 1} \tag{17}$$

Substituting Eq. (17) into Eq. (16), $\tau_\Phi$ is given by

$$\tau_\Phi = \frac{\sigma_1 - \sigma_3}{\frac{\partial \sigma_1}{\partial \sigma_3} + 1} \left( \frac{\partial \sigma_1}{\partial \sigma_3} \right)^{1/2} \tag{18}$$

According to Eqs. (17) and (18) and the triangle $AHB$ in Fig. 6, tg $\Phi$ can be represented as

$$\text{tg } \Phi = \frac{\tau_\Phi}{\sigma_\Phi - \sigma_3} = \left( \frac{\partial \sigma_1}{\partial \sigma_3} \right)^{1/2} \tag{19}$$

and the derivative of the Mohr envelope can be evaluated from

$$\frac{\partial \tau_\Phi}{\partial \sigma_\Phi} = \text{tg } \beta' . \tag{20}$$

Because $2\Phi = \beta' + \pi/2$ and tg $\beta' = -ctg\, 2\Phi$ with

$$\text{tg } 2\Phi = 2 \text{ tg } \Phi / (1 - \text{tg}^2 \Phi),$$

combining Eqs. (19) and (20) recovers Eq. (15). Using Eq. (13) and the definition of (9a), we have

$$\text{tg } 2\Phi = A (\sigma_1 + \sigma_3 + W_1/B)/2, \tag{21}$$

where $A = -2 K_2 B/K_1$. Consideration of Eqs. (21) and (15) enables the differential equation to be rewritten as

$$2 \left( \frac{d \sigma_1}{d \sigma_3} \right)^{1/2} + \frac{A}{2} \left( \sigma_1 + \sigma_3 + \frac{W_1}{B} \right) \left( \frac{d \sigma_1}{d \sigma_3} - 1 \right) = 0 \tag{22}$$

in which the full derivative is used since the extra condition of Eq. (21) is involved to remove $\tau_\Phi$ and $\sigma_\Phi$ from Eq. (22). As $W_1/B$ is constant

$$\frac{d\left(\sigma_1 + \frac{W_1}{B}\right)}{d\sigma_3} = \frac{d\bar{\sigma}_1}{d\sigma_3} = \frac{d\sigma_1}{d\sigma_3}$$

in which $\bar{\sigma}_1 = \sigma_1 + W_1/B$. Therefore, Eq. (22) becomes

$$2\left(\frac{d\bar{\sigma}_1}{d\sigma_3}\right)^{1/2} + \frac{A}{2}(\bar{\sigma}_1 + \sigma_3)\left(\frac{d\bar{\sigma}_1}{d\sigma_3} - 1\right) = 0. \tag{23}$$

Equation (23) is suitable for the stress regime corresponding to relation (9a). In the case of (9b), Eq. (13) can be rewritten as $\operatorname{tg} 2\Phi^0 = -K_2/K_1$ in which the notation $\Phi^\circ$ denotes the failure angle at $\sigma_1 + \sigma_3 = (1 - W_1)/B$. Hence, Eq. (15) is defined as

$$2\left(\frac{d\sigma_1}{d\sigma_3}\right)^{1/2} + \operatorname{tg} 2\Phi^0\left(\frac{d\sigma_1}{d\sigma_3} - 1\right) = 0. \tag{24}$$

The solutions to Eqs. (23) and (24) are derived in Appendix 3 and summarized as follows:

$$\tau_{\max} = \begin{cases} \frac{1}{A}\ln\left[\sqrt{1 + A^2(\sigma_m + W_1/2B)^2} + A(\sigma_m + W_1/2B)\right] - \frac{W_1}{2B} + \sigma_t, & -\frac{W_1}{2B} \le \sigma_m \le \frac{1 - W_1}{2B} \quad (25\,a) \\ -\cos 2\Phi^\circ\,\sigma_m + C, & \sigma_m > \frac{1 - W_1}{2B} \quad (25\,b) \end{cases}$$

where, following standard notation, $\sigma_m = (\sigma_1 + \sigma_3)/2$; $\tau_{\max} = (\sigma_1 - \sigma_3)/2$, and $C = \tau^0_{\max} + \cos 2\Phi^0\,((1 - W_1)/2B)$ in which $\tau^0_{\max}$ is the value of Eq. (25a) at $\sigma_m = (1 - W_1)/2B$. Tensile stress $\sigma_t$ in the criterion can be approximated by Eq. (30), given subsequently. Equations (A.3.15) and (A.3.16) from Appendix 3 may be used to calculate $\sigma_1$ and $\sigma_3$ at failure. Parameters, $A$, $B$, and $W_1$ in Eq. (25a) may be evaluated using Eq. (9a) requiring that data from only two independent strength tests be available.

## 4. Experimental Data

Parameters, $B$, $W_1$, and $A$ must be evaluated to calibrate the phenomenological model. Results from a series of triaxial tests on Daye marble are available, as presented in Table 1. All samples are 5 cm in diameter and 11 cm in height. For convenience, one set of strength data is chosen from a uniaxial tensile test: $\sigma_1 = 0$, $\sigma_3 = -\sigma_t$ (which is approximated by Eq. (30)) and $\Phi = \pi/2$; and an additional set of strength data is obtained for an auxiliary triaxial strength test: $\sigma_1^*$ = maximum compressive strength, $\sigma_3^*$ = confining stress, and $\Phi^*$ = failure angle. The star superscript denotes a measured value. Substituting into Eq. (9a) and solving the appropriate equation, $B$ and $W_1$ are respectively expressed by

$$B = W^*/(\sigma_1^* + \sigma_3^* + \sigma_t), \quad W_i = B\sigma_t \tag{26}$$

where $W^* = -K_1 \operatorname{tg} 2\Phi^*/K_2$. Similarly, the parameter $A$ is given by

$$A = -2K_2 B/K_1 = 2 \operatorname{tg} 2\Phi^*/(\sigma_1^* + \sigma_3^* + \sigma_t). \tag{27}$$

**Table 1.** Ultimate compressive strength as a function of confining stress for Daye marble

| Confining stress (kg/cm²) | Ultimate compressive strength (kg/cm²) | Failure angles (degree) |
|---|---|---|
| 0 | 962 | — |
| 100 | 1454 | 67 |
| 200 | 1934 | 65 |
| 300 | 2329 | 60 |
| 400 | 2464 | 58 |
| 500 | 2724 | 56 |
| 600 | 3080 | 52 |
| 700 | 3487 | 52 |
| 800 | 3536 | 50 |
| 900 | 3676 | 49 |
| 1000 | 4027 | 48 |

To establish the validity of the shear-band criterion, the following strength data from Table 1 are used as basic parameters: $\sigma_1^* = 1454$ (kg/cm²), $\sigma_3^* = 100$ (kg/cm²), and $\Phi^* = 67$ (degrees). Combining this with any one of the remaining data sets enables the full failure envelope to be determined as illustrated in Fig. 7. For $\sigma_3^* \leq 700$ (kg/cm²), an excellent correlation is obtained with the measured data where strengths are determined from Eqs. (A.3.15) and (A.3.16).

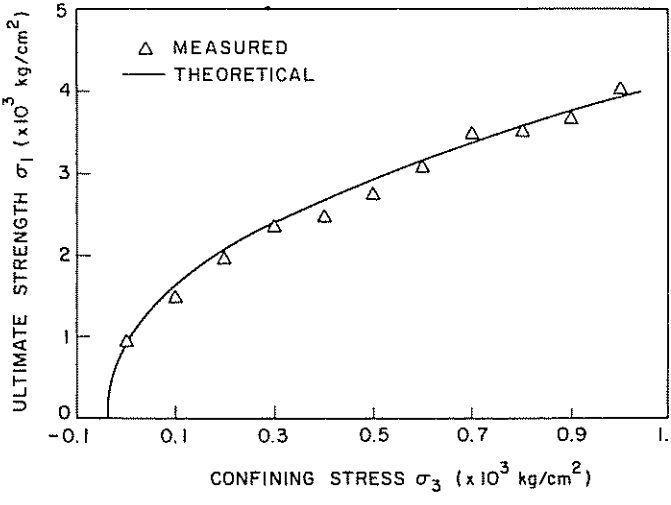


**Fig. 7.** Principle stresses at failure compared to the derived criterion for Daye marble

## 5. Summary and Conclusions

The preceding discussion illustrates several interesting points, notwithstanding the wedge model, that suggest the appropriateness of the model in simulating a realistic failure mechanism for brittle rock. These are summarized in the following:

### *5.1 Macroscopic Flaw Rigidity*

Substituting Eq. (26) into Eq. (9a) and rearranging yields

$$W/(\sigma_1 + \sigma_3 + \sigma_t) = W^*/(\sigma_3^* + \sigma_1^* + \sigma_t) = B. \tag{28}$$

Thus, Eq. (28) is only satisfied with $0 \leq W$ or $W^* \leq 1$ where the ratio of $W/(\sigma_1 + \sigma_3 + \sigma_t)$ is the constant $B$ and is unrelated to stress state at failure. $W^*$ may be evaluated through Eq. (13). In the special case of $W^* = 0$ (uniaxial tensile stress), $B$ is the limit value of Eq. (28) by taking

$$\lim_{\sigma_3 \to \sigma_t} \frac{W^*}{\sigma_3^* + \sigma_t} = B$$

as $W^*$ approaches zero. By definition, the dimensions of $B$ are $[M^{-1} LT^2]$ representing an equivalent modulus of rigidity for the flaw distribution. The constant $B$ represents the rigidity of flaw deformation in a statistical sense. For a specified rock, $B$ should be constant. When $\sigma_3 < 700$ kg/cm$^2$, $W^*$ is smaller than unity and the fissure rigidity $B$ is approximately constant with confining stress at failure as determined for Daye marble in Fig. 8.

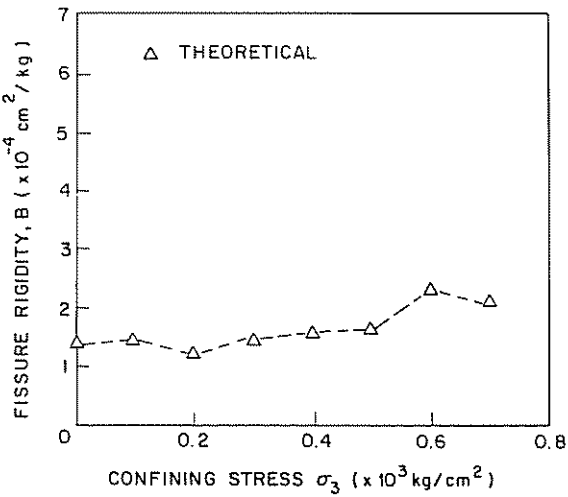


Fig. 8. Profile of fissure rigidity modulus $B$ for Daye marble

### 5.2 Relation of Failure Angle $\Phi$ and Stresses at Failure

Failure stresses and angle of failure are related. Combining Eqs. (13) and (26) with Eqs. (9a) and (14) yields

$$\Phi = \begin{cases} \frac{\pi}{2} - \frac{1}{2}\operatorname{arctg}\left[-\frac{A}{2}(\sigma_1+\sigma_3+\sigma_t)\right], & -\sigma_t \le \sigma_1+\sigma_3 \le \frac{1}{B}-\sigma_t \quad (29a) \\ \frac{\pi}{2} - \frac{1}{2}\operatorname{arctg}\left(\frac{K_2}{K_1}\right), & \sigma_1+\sigma_3 > \frac{1}{B}-\sigma_t. \quad (29b) \end{cases}$$

Equations (29a) and (29b) explain why failure angle $\Phi$ changes continuously with confining stress $\sigma_3$. As confining pressure $\sigma_3$ increases (such that $\sigma_1+\sigma_3 = 1/B - \sigma_t$ at failure) the coefficient of stress inhomogeneity, $W$, increases from a positive constant less than unity to unity. Correspondingly, the appropriate failure angle $\Phi$ defined in Eq. (29a) decreases to $\Phi = \pi/2 - 1/2 \operatorname{arctg}(K_2/K_1) \cong 51°$ as the lower limit. Experimental data closely fit this theoretical prediction further suggesting the appropriateness of the physical model. Macroscopic failure angles predicted from the theory are compared with experimental results for Daye marble in Fig. 9. For $\sigma_3 < 700$ kg/cm$^2$ there is close correspondence between theory and experiment with a slight degradation of fit with increasing confinement.

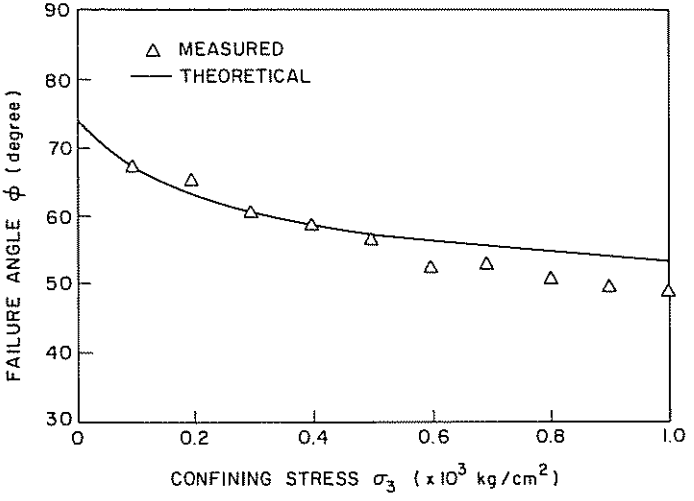


**Fig. 9.** Relation of failure angle $\Phi$ and confining stress $\sigma_3$ for Daye marble

### 5.3 Ratio $\sigma_c/\sigma_t$

The ratio of uniaxial compressive strength $\sigma_c$ to uniaxial tensile strength $\sigma_t$ reportedly varies in the range of 10 to 50 (Vutukuri et al., 1974). The ratios predicted by current failure criteria are normally lower than observed and material type independent. For example, $\sigma_c/\sigma_t = 5.8$ by the Coulomb

criterion, $\sigma_c/\sigma_t = 8$ by the Griffith criterion, and $\sigma_c/\sigma_t = 10$ by the McClintock and Walsh criterion (Vutukuri et al., 1974).

From either of Eqs. (A.3.7) or (A.3.8) in Appendix 3, the ratio may be obtained by setting $\sigma_1 = \sigma_1^* = \sigma_c$, $\sigma_3 = \sigma_3^* = 0$, and $\Phi = \Phi^* = \Phi_c$ where $\Phi_c$ is the angle of failure under uniaxial compression. Noting Eq. (27), Eq. (A.3.7) becomes,

$$\sigma_c = \frac{\sigma_c + \sigma_t}{2 \operatorname{tg} 2\Phi_c} \left[\operatorname{tg} 2\Phi_c + \ln (\operatorname{tg} 2\Phi_c - \sec 2\Phi_c)\right],$$

which upon further rearrangement becomes

$$\sigma_c/\sigma_t = (1 + D)/(1 - D) \tag{30}$$

where $D = \operatorname{ctg} 2\Phi_c \ln (\operatorname{tg} 2\Phi_c - \sec 2\Phi_c)$. Eq. (30) indicates that the ratio $\sigma_c/\sigma_t$ may differ with failure angles in uniaxial compression. The prediction appears to reasonably fit data. Although rocks often fail by splitting under conditions with very low or no confining pressure (Fairhurst and Cook, 1966), Woronow (1975) determines the preferred failure angle of brittle rock through use of prismatic specimens notched at varying inclinations and loaded to failure. Despite predicting the existence of a critical failure angle $\Phi_c$ in these experiments, limitations within conventional experimental conditions preclude direct measurement. However, using Eqs. (28) and (13), we may compute $\Phi_c$ from

$$\begin{aligned} \operatorname{tg} 2\Phi_c &= \operatorname{tg} 2\Phi^* (\sigma_c + \sigma_t)/(\sigma_1^* + \sigma_3^* + \sigma_t), \\ &\cong \operatorname{tg} 2\Phi^* \sigma_c/(\sigma_1^* + \sigma_3^*) \end{aligned} \tag{31}$$

in which $\sigma_t$ is omitted because $\sigma_c \gg \sigma_t$ and $\sigma_1^* + \sigma_3^* \gg \sigma_t$. If failure under uniaxial compression occurs on a plane inclined between $60° - 75°$, then from Eq. (31), the ratio $\sigma_c/\sigma_t$ is in the range of 7 to 40. Intuitively, the larger the flaw density within brittle rocks, the lower the uniaxial tensile strength. Conversely, the uniaxial compressive strength is little affected. Therefore, the ratio $\sigma_c/\sigma_t$ increases with increased initial microcrack density. In the present study, the stress inhomogeneity coefficient $W$ is inversely proportional to original microcrack density (see the definition of $W_1$ in Eq. (9a)) whereas the computed $\Phi_c$ is inversely proportional to $W$ (see Eq. (12)). As microcrack density increases, the predicted ratio $\sigma_c/\sigma_t$ of Eq. (30) also increases.

Peng and Johnson (1972) studied the crack distribution in Chelmsford granite and its effect on uniaxial tensile strength. With the flaws oriented parallel to the uniaxial direction, the tensile and compressive strengths were respectively 10 and 170 MPa. With a ninety degree rotation, the tensile failure stress is lowered to 5.9 MPa while the compressive strength remains unaltered at 182 MPa. Correspondingly, the $\sigma_c/\sigma_t$ ratios range between 17 and 31 as a result of flaw orientation. Utilizing the available strength data for Daye marble, the predicted $\sigma_c/\sigma_t$ ratio for $\sigma_3 = 100$ kg/cm$^2$ is 32, which is much higher than the spurious magnitudes calculated by other criteria.

The strength criterion is based upon a phenomenological model that considers failure to occur along a serrated shear plane. No prior assumption is made regarding the ultimate form of the failure envelope. Rather, the stress dependent nature of the failure process falls naturally from the analysis through consideration of the statical stress state within the failure zone. The ability to naturally replicate a power law failure envelope through phenomenological arguments alone defines the obvious utility of the approach. Although applied to failure of intact material in the previous, the method is equally applicable to discontinua.

## Appendix 1

Solution for closure at the ends of the minor axis of an elliptical cavity, as illustrated in Fig. 4, is available (eg. Sokolinbkoff, 1961) as

$$v = \frac{Rq}{E}(1-\mu^2)(1+n-2\cos 2\alpha), \tag{A.1.1}$$

where $v$ is displacement in the $y$ direction (Fig. 4), $R$ is mean radius of the ellipse, $R = (a+b)/2$, $n$ is the ellipticity, $n = (a-b)/(a+b)$, $q$ is the magnitude of uniaxial stress acting at an angle $\alpha$ to the major principal axis and the elastic constants are modulus, $E$, and Poisson ratio, $\mu$.

The four component stress states that apply are defined as:

$$q = \sigma_x;\ \alpha = 0 \tag{1}$$

$$q = \sigma_y;\ \alpha = \frac{\pi}{2} \tag{2}$$

$$q = \tau;\ \alpha = \frac{\pi}{4} \tag{3}$$

$$q = -\tau;\ \alpha = -\frac{\pi}{4}. \tag{4}$$

Superposition of stress states yields total displacement $\Delta b$ at the minor axis on the boundary as

$$\Delta b = v_{(1)} + v_{(2)} + v_{(3)} + v_{(4)} \tag{A.1.2}$$

$$\Delta b = [(2a+b)\sigma_y - b\sigma_x]\frac{(1-\mu^2)}{E}. \tag{A.1.3}$$

## Appendix 2

The derivative of Eq. (11) is

$$\frac{d\sigma_r}{d\Phi} = -\frac{K_1(\sigma_1-\sigma_3)}{2\sqrt{2}\,rmW}\left(\sin 2\Phi + \frac{K_2 W}{K_1}\cos 2\Phi\right). \tag{A.2.1}$$

Let $d\sigma_r/d\Phi = 0$, and the result becomes

$$\operatorname{tg} 2\Phi = -(K_2 W)/K_1. \tag{A.2.2}$$

Setting $2\varepsilon = \operatorname{arctg}[(K_2 W)/K_1]$ and noting that $0 \le K_2 W/K_1 < \infty$, we then have $\varepsilon < \pi/4$. Eq. (A.2.2) has two solutions for the extreme points as

$$\Phi = \pi/2 - \varepsilon \text{ and } \Phi = -\varepsilon$$

Using Eq. (A.2.2), the second order derivative of (11) yields

$$\frac{d^2\sigma_r}{d\Phi^2} = -\frac{K_1(\sigma_1-\sigma_3)}{\sqrt{2}\,rmW\cos 2\Phi} \tag{A.2.3}$$

and two cases for the solution of Eq. (A.2.2) must be considered to evaluate Eq. (A.2.3)

$$\Phi = \pi/2 - \varepsilon, \quad \frac{d^2\sigma_r}{d\Phi^2} = \frac{K_1(\sigma_1-\sigma_3)}{\sqrt{2}\,rmW\cos 2\varepsilon} > 0 \tag{A.2.4}$$

$$\Phi = -\varepsilon, \quad \frac{d^2\sigma_r}{d\Phi^2} = -\frac{K_1(\sigma_1-\sigma_3)}{\sqrt{2}\,rmW\cos 2\varepsilon} < 0 \tag{A.2.5}$$

Consequently, Eq. (A.2.4) suggests that $\sigma_r$ of Eq. (11) reaches a minimum value at $\Phi = \pi/2 - \varepsilon$. Substituting Eq. (A.2.2) into Eq. (11) and rearranging allows the stress $\sigma_r$ on the edge of wedge element to be determined

$$\sigma_r = \frac{K_1(\sigma_1+\sigma_3)}{4\sqrt{2}\,rmW}\left(1 + \frac{\sigma_1-\sigma_3}{(\sigma_1+\sigma_3)\cos 2\Phi}\right). \tag{A.2.6}$$

From Fig. 6, the line segments $\overline{O'Q}$ and $\overline{O'A}$ can be respectively evaluated as $\overline{O'Q} = -\cos 2\Phi(\sigma_1+\sigma_3)/2$ and $\overline{O'A} = (\sigma_1-\sigma_3)/2$.

Because $\Phi = (\pi/2) - \varepsilon$ and $\varepsilon < \pi/4$, the function $\cos 2\Phi$ is negative and $\overline{O'Q} < \overline{O'A}$, i. e.

$$(\sigma_1-\sigma_3)/((\sigma_1+\sigma_3)\cos 2\Phi) < -1. \tag{A.2.7}$$

Combining Eqs. (A.2.7) and (A.2.6) yields $(\sigma_r)_{\Phi=(\pi/2)-\varepsilon} < 0$. Then, $\Phi = (\pi/2) - \varepsilon$ is the minimum solution for $\sigma_r$. Moreover, from Eq. (A.2.2) stress inhomogeneity coefficient $W$ may be expressed as

$$W = -K_1 \operatorname{tg} 2\Phi/K_2. \tag{A.2.8}$$

## Appendix 3

In accordance with conventional notation, let $\bar{\sigma}_1 = y$, $\sigma_3 = x$, and $d\bar{\sigma}_1/d\sigma_3 = y'$, allowing the differential relationship of Eq. (23) to be expressed as

$$2\sqrt{y'} + \frac{1}{2} A (y + x)(y' - 1) = 0. \tag{A.3.1}$$

Rearranging Eq. (A.3.1) for $x$ and letting $y' = g$, we obtain

$$x = -y - 4\sqrt{g}/(A(g-1)), \tag{A.3.2}$$

Differentiation of (A.3.2) yields

$$\frac{1}{g} = \frac{2(1+g)}{A\sqrt{g}\,(g-1)^2}\frac{dg}{dy} - 1 \tag{A.3.3}$$

allowing $dy$ to be determined as

$$dy = \frac{2\sqrt{g}}{A(g-1)^2}\,dg. \tag{A.3.4}$$

Using the notation $\sqrt{g} = t$ and $dg = 2\,t dt$, integration of Eq. (A.3.4) yields

$$y = -\frac{2t}{A(t^2-1)} + \frac{1}{A}\ln\left(\frac{t-1}{t+1}\right) + C_1. \tag{A.3.5}$$

Combining Eqs. (A.3.2) and (A.3.5), we have

$$x = -\frac{2t}{A(t^2-1)} - \frac{1}{A}\ln\left(\frac{t-1}{t+1}\right) - C_1. \tag{A.3.6}$$

Observing from Eq. (19) that $2\,\mathrm{tg}\,\Phi/(1-\mathrm{tg}^2\,\Phi) = \mathrm{tg}\,2\Phi$ and $(\mathrm{tg}\,\Phi - 1)/(\mathrm{tg}\,\Phi + 1) = \mathrm{tg}\,2\Phi - \sec 2\Phi$, Eqs. (A.3.5) and (A.3.6) can be rearranged to give

$$\sigma_1 = \frac{1}{A}[\mathrm{tg}\,2\Phi + \ln(\mathrm{tg}\,2\Phi - \sec 2\Phi)] - \frac{W_1}{B} + C_1 \tag{A.3.7}$$

$$\sigma_3 = \frac{1}{A}[\mathrm{tg}\,2\Phi - \ln(\mathrm{tg}\,2\Phi - \sec 2\Phi)] - C_1. \tag{A.3.8}$$

For failure under uniaxial tension, the specimen characteristics are given by $\sigma_1 = 0$, $\sigma_3 = -\sigma_t$, and $\Phi = \pi/2$. Substituting these data into Eqs. (A.3.7) or (A.3.8), we obtain $C_1 = \sigma_t$. It is evident that Eqs. (A.3.7) and (A.3.8) can be transformed into

$$\sigma_m = \frac{1}{A}\,\mathrm{tg}\,2\Phi - \frac{W_1}{2B} \tag{A.3.9}$$

$$\tau_{\max} = \frac{1}{A}\ln(\mathrm{tg}\,2\Phi - \sec 2\Phi) - \frac{W_1}{2B} + \sigma_n \tag{A.3.10}$$

in which the notation $\sigma_m = (\sigma_1 + \sigma_3)/2$ and $\tau_{max} = (\sigma_1 - \sigma_3)/2$ is used. The criterion of Eq. (A.3.10) is valid over a limited range of $\sigma_m$ (see Eq. (9a)). From Eqs. (A.3.9) and (A.3.10), the expression for the failure criterion is

$$\tau_{max} = \frac{1}{A} \ln \left( \sqrt{1 + A^2 \left( \sigma_m + \frac{W_1}{2B} \right)^2} + A \left( \sigma_m + \frac{W_1}{2B} \right) \right) - \frac{W_1}{2B} + \sigma_t \tag{A.3.11}$$

Similarly, noting that $\frac{d\sigma_1}{d\sigma_3} = \frac{d\bar{\sigma}_1}{d\sigma_3} = y'$ Eq. (24) becomes

$$2\sqrt{y'} + \operatorname{tg} 2\Phi^0 (y' - 1) = 0. \tag{A.3.12}$$

The dual solutions for the quadratic relationship (A.3.12) are

$$(\sqrt{y'})_1 = \frac{-2 + \sqrt{4 + 4 \operatorname{tg}^2 2\Phi^0}}{2 \operatorname{tg} 2\Phi^0} = \operatorname{tg} \Phi^0 > 0$$

$$(\sqrt{y'})_2 = \frac{-2 - \sqrt{4 + 4 \operatorname{tg}^2 2\Phi^0}}{2 \operatorname{tg} 2\Phi^0} = -c \operatorname{tg} \Phi^0 < 0.$$

Therefore, $(\sqrt{y'})_1$ is the solution for Eq. (A.3.12), i. e., $y' = \operatorname{tg}^2 \Phi^0$. After integrating $y' = \operatorname{tg}^2 \Phi^0$, results can be inverted to give

$$\sigma_1 = \operatorname{tg}^2 \Phi^0 \, \sigma_3 + C \tag{A.3.13}$$

Rearranging Eq. (A.3.13), we obtain

$$\tau_{max} = -\cos 2\Phi^0 \cdot \sigma_m + C, \tag{A.3.14}$$

The constant $C$ can be computed from the condition that $\tau_{max} = \tau^0_{max}$ at $\sigma_m = (1 - W_1)/2B$ in Eq. (A.3.10):

$$C = \tau^0_{max} + \cos 2\Phi^0 \frac{1 - W_1}{2B}. \tag{A.3.14a}$$

For convenience a similar expression for the failure criterion in Eq. (A.3.13) may be obtained from Eq. (A.3.11) as

$$\sigma_1 = \sigma_m + \tau_{max} \tag{A.3.15}$$

$$\sigma_3 = \sigma_m - \tau_{max}. \tag{A.3.16}$$

## References

Batzle, M., Simmons, G., Siegfried, R. (1979) Direct observation of fracture closure in rocks under stress. EOS Trans. 60, 380.

Bieniawski, Z. T. (1966): Mechanism of brittle fracture of rock. CSIR Report RMEG 580, Pretoria.

Bombolakis, E. G. (1968): Photoelastic study of initial stages of brittle fracture in compression. Tectonophysics 6, 461—473.

Brace, W. F., Bombolakis, E. G. (1963): A note on brittle crack growth in compression. J. Geophys. Res. 68, 3709—3713.

Brace, W. F., Paulding, B. W., Scholz, C. (1966): Dilatancy in the fracture of crystalline rocks. J. Geophys. Res. 71, 3939—3952.

Brady, B. T. (1969a): A statistical theory of brittle fracture. Part I. Int. J. Rock Mech. Min. Sci. and Geomech. Abstr. 6, 21—42.

Brady, B. T. (1969b): A statistical theory of brittle fracture. Part II. Int. J. Rock Mech. Min. Sci. and Geomech. Abstr. 6, 285—300.

Dey, T. N., Wang, C.-Y. (1981): Some mechanics of microcrack growth and interaction in compressive rock failure. Int. J. Rock Mech. Min. Sci. and Geomech. Abstr. 18, 199—209.

Fairhurst, C., Cook, N. G. W. (1966): The phenomenon of rock splitting parallel to the direction of maximum compression in the neighborhood of a surface. In: Proc. 1st Int. Congress Int. Soc. Rock Mech. Liston, 687—692.

Fonseka, G. M., Murrell, S. A. F., Barnes, P. (1985): Scanning electron microscope and acoustic emission studies of crack development in rocks. Int. J. Rock Mech. Min. Sci. and Geomech. Abstr. 22, 273—289.

Griffith, A. A. (1921): The phenomena of rupture and flow in solids. Philosophical Transactions 221, 163—198.

Griffith, A. A. (1924): Theory of rupture. In: Proc. 1st Int. Congress on Appl. Mechanics, Delft, 55—64.

Hallbauer, D. K., Wager, H., Cook, N. G. W. (1973): Some observations concerning the microscope and mechanical behavior of quartzite specimens in stiff triaxial compression tests. Int. J. Rock Mech. Min. Sci. and Geomech. Abstr. 10, 713—726.

Hoek, E., Bieniawski, Z. T. (1965): Brittle fracture propagation in rock under compression. Int. J. Fracture Mech. 1, 137—155.

Janach, W. (1977): Failure of granite under compression. Int. J. Rock Mech. Min. Sci. and Geomech. Abstr. 14, 209—215.

Kranz, R. L. (1979a): Crack growth and development during creep in Barre granite. Int. J. Rock Mech. Min. Sci. and Geomech. Abstr. 16, 23—36.

Kranz, R. L. (1979b): Crack-crack and crack-pore interactions in stressed granite. Int. J. Rock Mech. Min. Sci. and Geomech. Abstr. 16, 37—48.

Liu, H. P., Livanos, A. C. R. (1976): Dilatancy and precursory bulging along incipient fracture zones in uniaxially compressed Westerly granite. J. Geophys. Res. 81, 3495—3510.

Lundborg, N. A. (1974): A statistical theory of polyaxial strength of materials. In: Proc. 3rd Int. Congress Int. Soc. Rock Mech., Denver, 180—185.

McClintock, F. A., Walsh, J. B. (1962): Friction on Griffith cracks in rocks under pressure. In: Proc. 4th U.S. National Congress on Applied Mechanics, Vol. 2, 1015—1021.

Nesetova, V., Lajtai, E. Z. (1973): Fracture from compressive stress concentrations around elastic flaws. Int. J. Rock Mech. Min. Sci. and Geomech. Abstr. 10, 265—284.

Peng, S. D., Johnson, A. M. (1972): Crack growth and faulting in cylindrical specimens of Chelmsford granite. Int. J. Rock Mech. Min. Sci. 9, 37—86.

Scholz, C. H. (1968a): Microfracturing, aftershocks and seismicity. Bull. Seism. Soc. Am. 58, 1117—1130.

Scholz, C. H. (1968b): Macrofracturing and the inelastic deformation of rock in compression. J. Geophys. Res. 73, 1417—1432.

Sokolinkoff, I. S. (1961): Mathematical theory of elasticity, 476 pp. J. Geophys. Res., 4237—4292.

Swain, M. V., Lawn, B. R., Burns, S. J. (1974): Cleavage step deformation in brittle solids. J. Mater. Sci. 9, 175—183.

Tapponnier, P., Brace, W. F. (1976): Development of stress induced microcracks in Westerly granite. Int. J. Rock Mech. Min. Sci. and Geomech. Abstr. 13, 102—113.

Timoshenko, S. P., Goodier, J. N. (1970): Theory of elasticity. McGraw-Hill, New York, 109—112.

Vutukuri, V. S., Lama, R. D., Saluja, S. S. (1974): Handbook on mechanical properties of rocks, Vol. I, Trans. Tech. Publ. Clausthal.

Wang, T. F. (1982): Micromechanics of faulting in Westerly granite. Int. J. Rock Mech. Min. Sci. and Geomech. Abstr. 19, 49—64.

Wiebols, G. A., Cook, N. G. W. (1968): An energy criterion for the strength of rock in polyaxial compression. Int. J. Rock Mech. Min. Sci. and Geomech. Abstr. 5, 529—549.

Woronow, A. (1975): A new technique for determining the preferred failure angle of brittle rock. Int. J. Rock Mech. Min. Sci. and Geomech. Abstr. 12, 289—293.

Wu, F. T., Thomsen, L. (1975): Microfracturing and deformation of Westerly granite under creep condition. Int. J. Rock Mech. Min. Sci. and Geomech. Abstr. 12, 167—173.

**Authors' address:** Dr. Z. Ouyang, Department of Mining Engineering, Wuhan Steel and Iron University, Wuhan, 430081, People's Republic of China; Dr. D. Elsworth, Department of Mineral Engineering, Pennsylvania State University, University Park, PA 16802, U.S.A. and Waterloo Centre for Groundwater Research, University of Waterloo, Waterloo, Ontario N2L 3G1, Canada.